Evaluation of WRF Cloud Microphysics Schemes Using Radar Observations

KI-HONG MIN

Department of Astronomy and Atmospheric Sciences, Kyungpook National University, Daegu, South Korea, and Department of Earth, Atmospheric, and Planetary Sciences, Purdue University, West Lafayette, Indiana

SUNHEE CHOO

Department of Astronomy and Atmospheric Sciences, Kyungpook National University, Daegu, South Korea

DAEHYUNG LEE AND GYUWON LEE

Department of Astronomy and Atmospheric Sciences, and Research and Training Team for Future Creative Astrophysicists and Cosmologists (BK21 Plus Program), Kyungpook National University, Daegu, South Korea

(Manuscript received 20 August 2014, in final form 13 July 2015)

ABSTRACT

The Korea Meteorological Administration (KMA) implemented a 10-yr project to develop its own global model (GM) by 2020. To reflect the complex topography and unique weather characteristics of the Korean Peninsula, a high-resolution model with accurate physics and input data is required. The WRF single-moment 6-class microphysics scheme (WSM6) and WRF double-moment 6-class microphysics scheme (WDM6) that will be implemented in the Korea GM (KGM) are evaluated. Comparisons of the contoured frequency by altitude diagram (CFAD), time–height cross sections, and vertical profiles of hydrometeors are utilized to assess the two schemes in simulating summer monsoon and convective precipitation cases over the Korean Peninsula during 2011. The results show that WSM6 and WDM6 overestimate the height of the melting level and bright band as compared to radar observations. However, the accuracy of WDM6 is in better agreement with radar observations. This is attributed to the difference in the sedimentation process simulated by the additional second-moment total number concentrations of liquid-phase particles in WDM6. WDM6 creates larger raindrops and higher relative humidity beneath the melting layer, allowing the scheme to simulate a more realistic reflectivity profile than WSM6 for the summer monsoon case. However, for the convective case, both schemes underestimate the precipitation and there is resolution dependence in the WRF Model's ability to simulate convective precipitation.

1. Introduction

The representation of clouds in mesoscale numerical weather prediction (NWP) models is one of the areas with major uncertainties in current predictions of short- and long-term weather and future climate. Cloud microphysics parameterization is required in most NWP models because a sophisticated, explicit prediction of the evolution of cloud microstructure is either impossible or impractical even with the most advanced computing resources. Cloud microphysics schemes calculate the precipitation amount and intensity and simulate the growth and development of water droplets in warm and cold rain processes. In addition, they redistribute the energy, momentum, and moisture among model grid points and interact closely with radiation processes and the atmospheric boundary layer.

In the early stages, cloud parameterization schemes diagnosed ice and water droplets using temperature profiles and determined the amount of cloud using only moisture profiles (Sundqvist 1978; Smith 1990). However, these approximations had many issues, and as high-resolution NWP became available, the traditional diagnostic approach has shown to have many limitations. Recently, increases in computing power and NWP technology have led to more accurate and detailed descriptions of cloud microphysical processes and the

Corresponding author address: Gyuwon Lee, Dept. of Astronomy and Atmospheric Sciences, Kyungpook National University, 80 Daehak-ro Buk-gu, Daegu 702-701, South Korea.
E-mail: gyuwon@knu.ac.kr

DOI: 10.1175/WAF-D-14-00095.1

trend has been toward prognostically calculating hydrometeor types and sizes explicitly (Wilson and Ballard 1999; Hong et al. 2004; Morrison and Gettelman 2008; Lim and Hong 2010).

Among the numerous microphysics options, Hong and Lim (2006) improved the Weather Research and Forecasting (WRF) Model single-moment 5-class microphysics scheme (WSM5) to include graupel as another prognostic variable [WRF single-moment 6-class microphysics scheme (WSM6)]. They showed that the evolution of simulated precipitation with WSM6 is similar to that from WSM5 in a low-resolution grid, but at high resolutions the amount of rainfall increases and the peak intensity becomes stronger as the number of hydrometeors increases. Furthermore, Lim and Hong (2010) developed a double-moment bulk cloud microphysics scheme [WRF double-moment 6-class microphysics scheme (WDM6)] that predicts the number concentrations for cloud, rainwater, and cloud condensation nuclei (CCN), as well as predicting the six hydrometeor types (water vapor, cloud droplets, cloud ice, snow, rain, and graupel). WDM6 has been reported to reduce light precipitation and increase moderate precipitation, reducing the systematic bias of WSM6 (Hong et al. 2010).

A recent trend in evaluating NWP models is to use data obtained from remote sensing equipment such as satellites (*CloudSat*), radars, and *Cloud–Aerosol Lidar and Infrared Pathfinder Satellite Observations* (*CALIPSO*; Konsta et al. 2012). The use of these active sensors makes it possible to evaluate the three-dimensional structure of clouds and precipitation. Chepfer et al. (2008) used lidar and a *CALIPSO* simulator to evaluate the vertical structure of clouds in a GCM. Haynes et al. (2007) used radar observations from *CloudSat* and a radar simulator to compare observed and simulated reflectivity profiles. Stoelinga (2005) defines simulated reflectivity (SR) as the equivalent radar reflectivity calculated from hydrometeors in cloud microphysics schemes. Displaying outputs with SR are becoming popular because it provides many advantages compared to NWP precipitation forecasts. Koch et al. (2005) mentioned that SR is easier to verify with observed radar composites in real time by weather forecasters. In addition, using simulated reflectivity products to compare model fields with radar has advantages over radar-estimated precipitation fields because there is less uncertainty involved in the calculation of reflectivity from the model than precipitation from radar (Koch et al. 2005; Molthan and Colle 2012). Finally, an additional advantage of using SR is that the structures, motions, and evolutions of storm signatures are more recognizable in radar reflectivity fields than in any other meteorological variables (Stoelinga 2005). In this regard, SR allows one to more easily see detailed meso- and storm-scale structures forecasted by finer-resolution NWP models (Kain et al. 2008; Hitchens et al. 2012).

Such research has only recently begun in South Korea with the availability of quality controlled radar data and the need for more accurate weather information has become increasingly crucial with increases in local severe weather activities (G. Lee 2012). In addition, the Korea Meteorological Administration (KMA) implemented a 10-yr project to develop its own global model (GM) by 2020. This global model is being developed at the Korea Institute of Atmospheric Prediction Systems (KIAPS), which is a KMA-funded nonprofit research and development institute that was established in 2011. The goal is to develop a next-generation operational global NWP system with 10-km resolution or higher, which can be used for global modeling as well as for generating forecasts for local areas, optimized to the topographic and meteorological features of the Korean Peninsula (Kwon et al. 2014). The KIAPS Integrated Model with the Spectral Element Hydrostatic dynamical core (KIMSH) has a cubed-sphere grid structure similar to that in the National Center for Atmospheric Research's (NCAR) Community Atmosphere Model Spectral Element (CAM-SE) and includes a local ensemble transform Kalman filter (LETKF) data assimilation system. The physics parameterization schemes have been developed mostly in house or by scientists affiliated with KIAPS.

To reflect the complex topography and unique weather characteristics across the Korean Peninsula, a high-resolution model with accurate physics and input data is required. The purpose of this study is to evaluate the cloud microphysics schemes that will be used in KIMSH and to determine their strengths and weaknesses. We compare the melting layer and brightband signatures obtained from ground-based KMA S-band Doppler radar with WSM6 and WDM6 that will be adapted in the Korea GM (KGM). Comparisons of contoured frequency by altitude diagrams (CFAD), time–height cross sections, and vertical profiles of hydrometeors are utilized to assess the two schemes in simulating the summer monsoon and convective precipitation cases during 2011 across the Korean Peninsula.

2. Method and data

A large amount of information can be extracted from ground-based weather surveillance radar. When analyzing stratiform precipitation radar data, a rapid enhancement and decay of reflectivity referred to as bright bands (BB) can be observed. BBs represent enhanced reflectivity regions near the 0°C isotherm layer caused by changes in the dielectric constant and the backscattering

TABLE 1. Selected configuration and parameterization schemes used in the WRF Model, version 3.5, simulations.

Cumulus parameterization	Kain–Fritsch (5 min)
Microphysics	WSM6 WDM6
Longwave radiation	RRTM
Shortwave radiation	Dudhia (10 min)
Surface-layer physics	Monin–Obukhov similarity
Land surface	Noah LSM
PBL	YSU scheme
Moisture	Positive-definite advection
Horizontal grid spacing	36 km (D01), 12 km (D02), and 4 km (D03)
Vertical level	60 (model top at 50 hPa)
Initial and boundary conditions	1° × 1° FNL fields obtained from NCEP/Environmental Modeling Center (EMC)

cross sections of melting hydrometeors (Austin and Bemis 1950). Aggregation of snowflakes above and within the melting layer leads to the formation of large particles and yields maximum radar reflectivities by up to a factor of 5 (Stewart et al. 1984). The height of a BB provides information on the 0°C isotherm layer and plays an important role in characterizing different hydrometeor types (Fabry and Zawadzki 1995; Liu and Chandrasekar 2000). The monitoring and understanding of BBs from radar observations can help improve radar rainfall estimation, help in identifying cloud microphysical processes, and aid in forecasting aircraft icing (Smith 1986; Smyth and Illingworth 1998; Seo et al. 2000; Zawadzki et al. 2001).

The method we employ to calculate the simulated radar reflectivity from the WRF Model follows the recommendations provided by Koch et al. (2005) and Stoelinga (2005). Their papers discussed the use of simulated reflectivity products to compare model fields with radar observations and they reported that this comparison has advantages over radar-estimated precipitation fields because there is less uncertainty involved in the calculation of reflectivity. Therefore, to compare WSM6 and WDM6 using radar reflectivity data, we analyzed CFAD for BB detection and used time–height cross sections to supplement CFAD, which has no time information. To further understand the cloud microphysics mechanism responsible for the differences in the two schemes, we investigated the vertical profiles of hydrometeors and temperature with humidity profiles. Radar data were quality controlled using a fuzzy logic algorithm developed at the Kyungpook National University (KNU) to remove anomalous propagation (AP) and nonmeteorological echoes such as ground clutter, sea clutter, and chaffs.

TABLE 2. List of selected cases for this study.

Case No.	Period	Characteristics
1	24–25 Jun 2011	Summer monsoon
2	14 Aug 2011	Convective
3	3–4 Jul 2011	Summer monsoon
4	11 Aug 2011	Convective

a. Calculation of radar-equivalent reflectivity factor

The equivalent reflectivity factor in an NWP model is computed from the forecast mixing ratios of grid-resolved hydrometeor species, assuming Rayleigh scattering by spherical particles of known density and size distribution (Sun and Crook 1997). This radar SR is calculated using the ARW post algorithm developed by Stoelinga (2005). A brief explanation of the calculation is described below.

The size distribution of actual diameter D of the particles is assumed to follow an exponential distribution of the form

$$N(D) = N_0 e^{-\lambda D}, \tag{1}$$

where N_0 represents constants of 8×10^6, 2×10^7, and $4 \times 10^6\,\mathrm{m}^{-4}$ for rain, snow, and graupel, respectively, and λ is a slope factor. In this study with mixed-phase bulk microphysical schemes, the intercept parameter for snow N_{0_S} was changed from a constant value to a temperature-dependent value (where T_c is the temperature in Celsius) as described in Thompson et al. (2008). Warmer temperatures yield lower N_{0_S} to account for the effects of enhanced aggregation:

$$N_{0_S} = 2 \times 10^6 e^{-0.12 T_c}. \tag{2}$$

The equivalent reflectivity factor Z_e ($\mathrm{m}^6\,\mathrm{m}^{-3}$), which is the sixth moment of the size distribution, is given by

$$Z_e = \Gamma(7) N_0 \lambda^{-7}, \tag{3}$$

where Γ is the gamma function. The equivalent reflectivity value associated with each hydrometeor mixing ratio is then calculated at grid points, and the values can be summed together to yield a total equivalent reflectivity factor:

$$Z_t = 10 \log_{10}(Z_e), \tag{4}$$

where Z_e is multiplied by 10^{18} to acquire new units ($\mathrm{mm}^6\,\mathrm{m}^{-3}$) and Z_t has units of decibels (dBZ). This is the final quantity that is calculated and displayed in the ARW post algorithm.

The current SR algorithm only accounts for Rayleigh scattering, but should be sufficient for S-band 10-cm

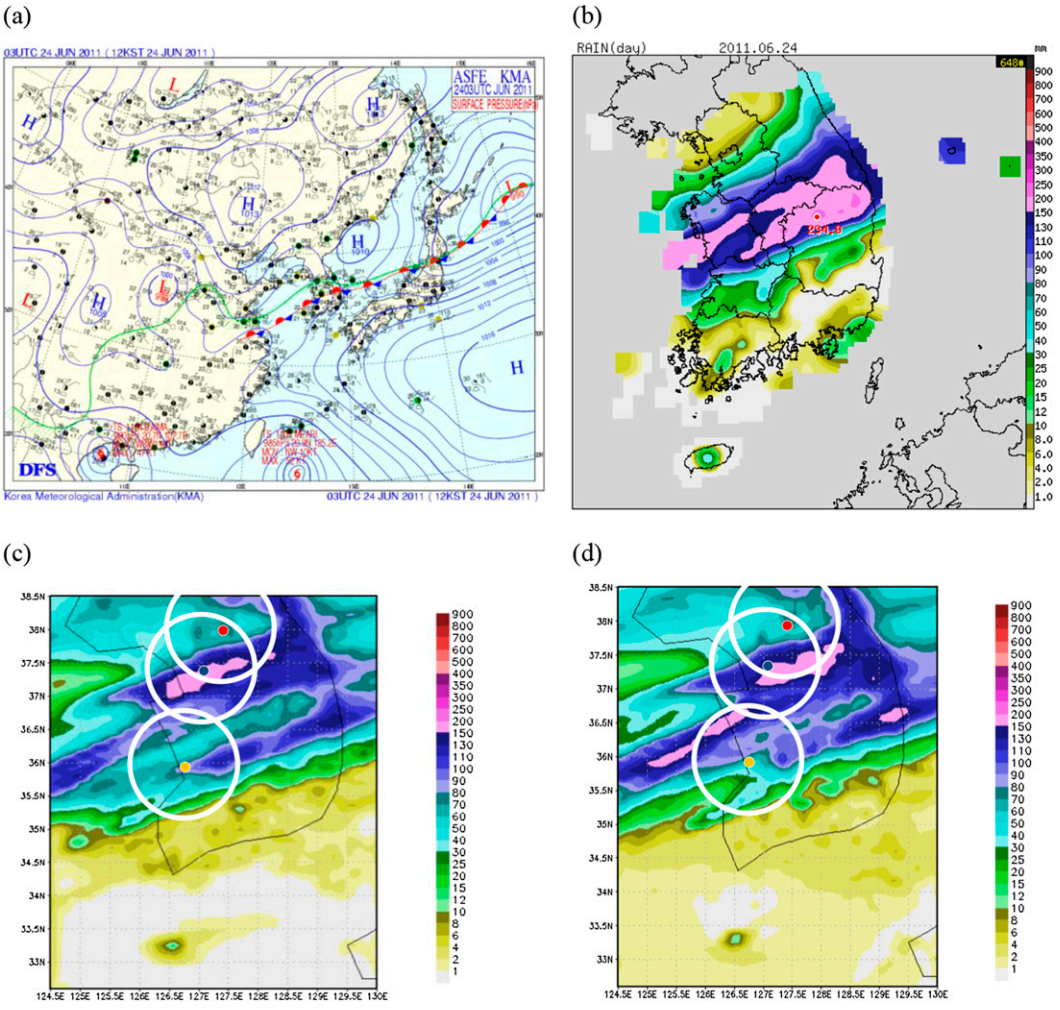

FIG. 1. Representative images from case 1 (from 0900 UTC 23 Jun to 2100 UTC 24 Jun 2011). (a) Surface weather chart at 0300 UTC 24 Jun. The 24-h accumulated precipitation on 24 Jun from (b) AWS observations and from (c) WSM6 and (d) WDM6 simulations. In (c),(d), the locations of the three radar sites chosen for this study are represented by colored dots (GDK in red, KWK in blue, and KSN in yellow) along with the 100-km-radius circle (white).

weather radars like the KMA Doppler radar. This is because the spectrum band is much longer than most of the diameters of the observed particles, and Rayleigh scattering is the dominant scattering regime.

b. WRF Model setup

A comprehensive atmospheric form of ARW (version 3.5; Skamarock et al. 2008), is used for this study. The model is widely used in meteorological research and applications, and is a full-physics, 3D nonhydrostatic model that has prognostic equations for wind, temperature, surface pressure, turbulent kinetic energy (TKE), and all phases of water (including vapor, cloud water, ice, snow, rain, and supercooled water). The configuration of the WRF Model used here includes single- and double-moment 6-class cloud microphysics schemes; Rapid Radiative Transfer Model (RRTM) longwave and Dudhia shortwave radiation schemes; the National Centers for Environmental Prediction (NCEP), Oregon State University, U.S. Air Force, and Hydrologic Research Laboratory Noah land surface model; the Yonsei University (YSU) TKE scheme for the planetary boundary layer; and the Kain–Fritsch (KF) convection scheme with adaptive time stepping for the two outer domains (Table 1).

The WRF Model domain is nested twice to achieve 4-km resolution from 1° NCEP Final Analysis (FNL) data. The 4-km resolution is needed to account for the complexity of the local topography and to compare directly with radar data. The mother domain (D01) is configured to allow large-scale monsoon features to propagate appropriately over the Korean Peninsula. The second domain (D02) is used to compare resolution dependency

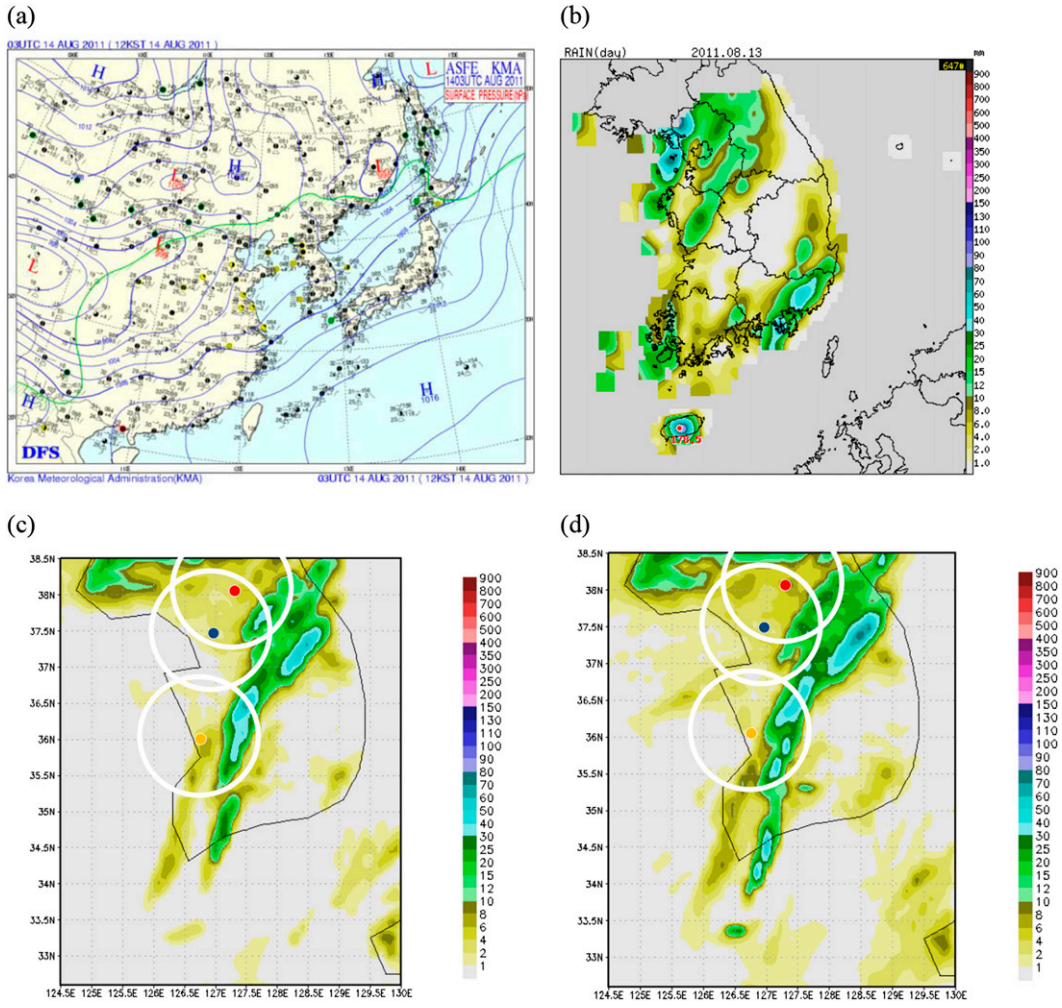

FIG. 2. Representative images from case 2 (from 2100 UTC 12 Aug to 1800 UTC 14 Aug 2011). (a) Surface weather chart at 0300 UTC 14 Aug. The 24-h accumulated precipitation on 13 Aug from (b) AWS observations and from (c) WSM6 and (d) WDM6 simulations. In (c),(d), the locations of the three radar sites chosen for this study are represented by colored dots (GDK in red, KWK in blue, and KSN in yellow) along with the 100-km-radius circle (white).

between D02 and the third domain (D03) model runs. There are 60 vertical levels and 130 × 169 grid points in D03, where most of the analyses are performed. WSM6 and WDM6 allow for six types of hydrometeors (specific humidity q): q_{vapor}, q_{rain}, q_{ice}, q_{cloud}, q_{snow}, and q_{graupel} to be predicted in the model. WDM6 differs from WSM6 in that it has three more prognostic variables of CCN and number concentrations of cloud droplets and rain. Among the six hydrometeors, q_{rain}, q_{snow}, and q_{graupel} are used to calculate the reflectivity.

To evaluate the simulations of WSM6 and WDM6, we compared simulated versus observed KMA radar reflectivity results. BB effects are added by scaling the SR of snow and graupel at temperatures greater than 0°C. The creation of a liquid skin on melting snowflakes increases their dielectric factor to the liquid value K_l. Thus, a scaling factor is applied by setting the dielectric ratio of ice and liquid ($|K_i|^2/|K_l|^2$) to 1 in the calculation of equivalent reflectivity for snow and graupel in regions where the temperature $T > 0$°C (Stoelinga 2005). Although SR is not the same as the precipitation rate at the surface, it gives insight into the simulated and observed precipitation at different spatiotemporal scales for diagnostic evaluation of cloud hydrometeor contents (Wright et al. 2013).

c. Selected cases

We selected four cases for the evaluation of WSM6 and WDM6, among which we show two representative cases for comparison. The four selected cases are summarized in Table 2. Case 1 is the summer monsoon known as the changma front in Korea that occurred toward the end of June and early July 2011. The 12-h

TABLE 3. Characteristics and locations of the S-band Doppler radars.

	KWK	GDK	KSN	Mount Bisl (dual polarization)
Lat (N)	37.4439°	38.1172°	36.0125°	35.6938°
Lon (E)	126.9639°	127.4339°	126.7839°	128.535°
Elev (m)	641	1061	234	1089
Range (km)	240.25	250	240.25	100
Dual pulse repetition frequency	600/400	600/400	600/400	1000/700
Nyquist velocity ($m\,s^{-1}$)	33.1	30.9	32.9	—
Gate size (m)	250	250	250	150
Beamwidth	0.9°	1°	1°	0.95°
Wavelength (cm)	11	10.4	11	10
No. of scan levels	13	12	15	6
No. of bins	960	1000	957	833
Mean bias (dB)	−4.46	−6.02	−6.69	—

accumulated rainfall totals from the automatic weather stations (AWSs), WSM6, and WDM6 for case 1 are shown in Fig. 1. The changma front propagated southward from the center of the Korean Peninsula and the major precipitation band was located between Seoul (37.5°N, 126.7°E) and Kunsan (36°N, 126.7°E), South Korea.

Case 2 is a scattered convection event that occurred after the end of the summer monsoon in mid-August because of atmospheric instability (Fig. 2). Convective cells repeatedly developed, matured, and dissipated over South Korea and produced convective precipitation in the western half of the Korean Peninsula. Case 3 is another summer monsoon simulation and case 4 is a convective precipitation simulation used to determine the fidelity of the results obtained in this study.

d. KMA radar data

Radar data were quality controlled using a fuzzy logic algorithm developed at KNU to remove AP and nonmeteorological echoes, such as ground clutter, sea clutter, and chaffs (Cho et al. 2006; Ye 2012). In addition,

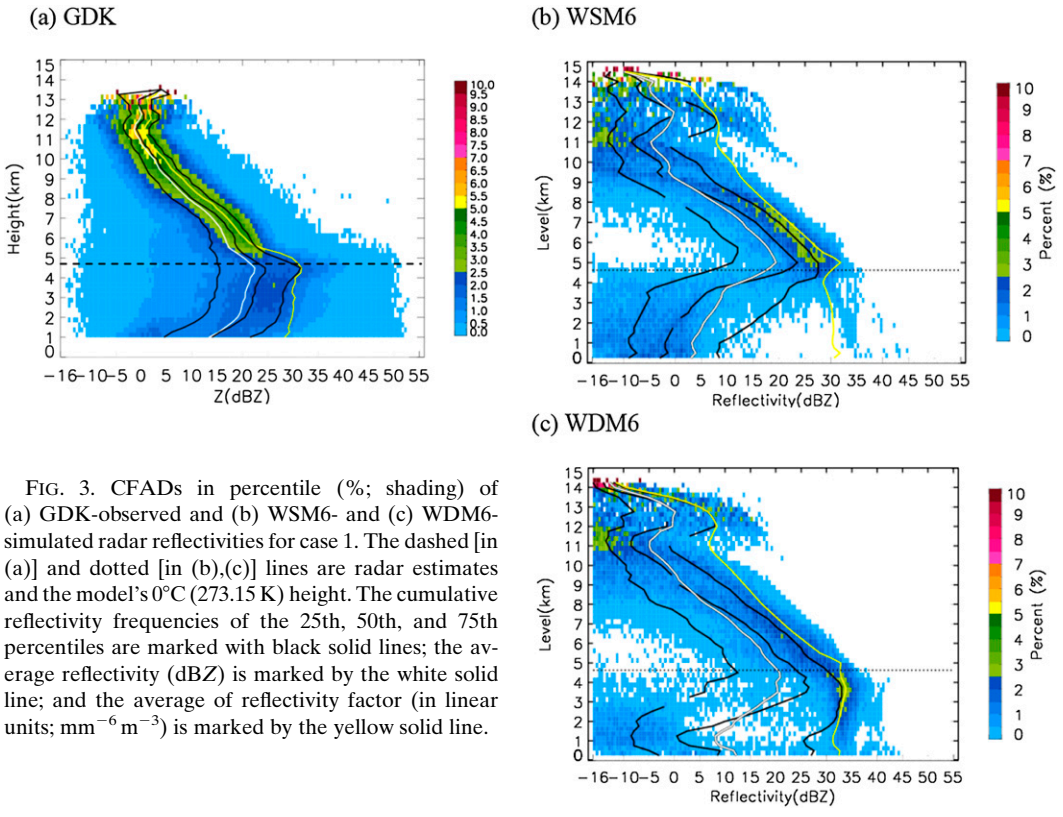

FIG. 3. CFADs in percentile (%; shading) of (a) GDK-observed and (b) WSM6- and (c) WDM6-simulated radar reflectivities for case 1. The dashed [in (a)] and dotted [in (b),(c)] lines are radar estimates and the model's 0°C (273.15 K) height. The cumulative reflectivity frequencies of the 25th, 50th, and 75th percentiles are marked with black solid lines; the average reflectivity (dBZ) is marked by the white solid line; and the average of reflectivity factor (in linear units; $mm^{-6}\,m^{-3}$) is marked by the yellow solid line.

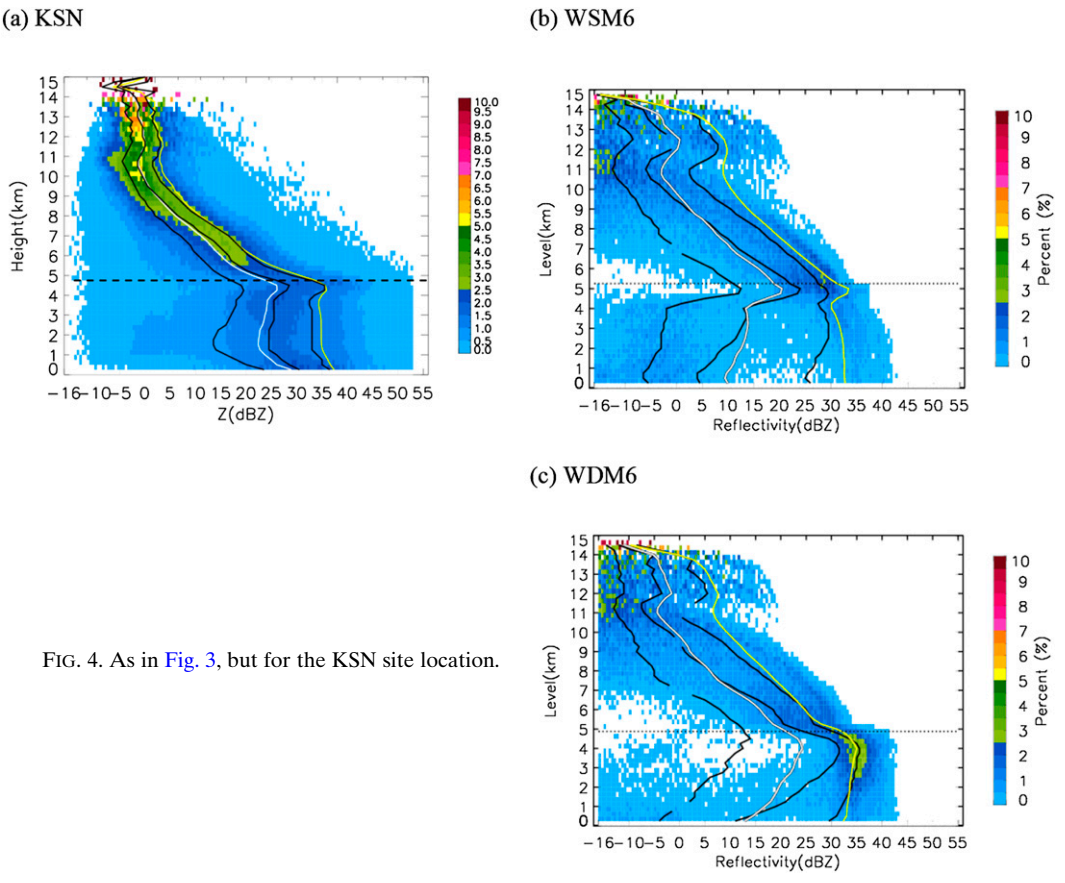

FIG. 4. As in Fig. 3, but for the KSN site location.

the systematic error (mean bias) of each radar site shown in Table 3 was corrected. The bias is corrected by comparing a 2-yr climatology (2009–10) of reflectivity between the Mount Bisl dual-polarized Doppler radar and the three radars [Gwangdeuk-san (GDK), Kwanak-san (KWK), and Kunsan (KSN)]. Detailed characteristics of radars used in this study are summarized in Table 3.

Radar data were converted from the polar coordinate system to the Cartesian coordinate in constant-altitude plan position indicator (CAPPI) to compare the radar reflectivity with that of the WRF Model. The horizontal and vertical resolutions of 4 km and 250 m, respectively, are identical to those of the WRF Model grids. Because of the curvature of the earth, the plan position indicator beam altitude increases as the distance increases; that is, even when the beam is at the 0°-elevation plane, the beam shoots over 1 km from the farthest point on the ground. The beamwidth is also widened, which can further contaminate the signal by averaging the precipitation from different regions at large distances from the radar site. The beamwidth W at distance R with elevation angle θ is calculated from $W = R\sin\theta \approx R\theta = R(2\pi/360)$. For $R = 100$ km, $W = 1.745$ km. Each point in the vertical is filled assuming a Gaussian distribution and an inverse distance–weighted interpolation is performed to achieve the 250-m vertical resolution. Thus, only a horizontal distance of 100-km radius from the radar was used in this study.

3. Results

a. CFAD

The CFAD summarizes the frequency distribution information about a variable in a given radar echo volume in a single contour plot (Yuter and Houze 1995). To obtain such a plot, the data are stratified by altitude only, and the horizontal locations of the data are ignored. The frequency of occurrence of reflectivity at a given height is retained. The CFAD preserves the information in the frequency distribution. The CFAD also overcomes the mismatch in space scales and time scales of radar data. This method is useful for visualizing radar data that would not be sensitive to the interpretation at a single point in the volume.

In this study, we analyzed the radar and simulated reflectivities of -16 dBZ or greater with a 0.5-dBZ

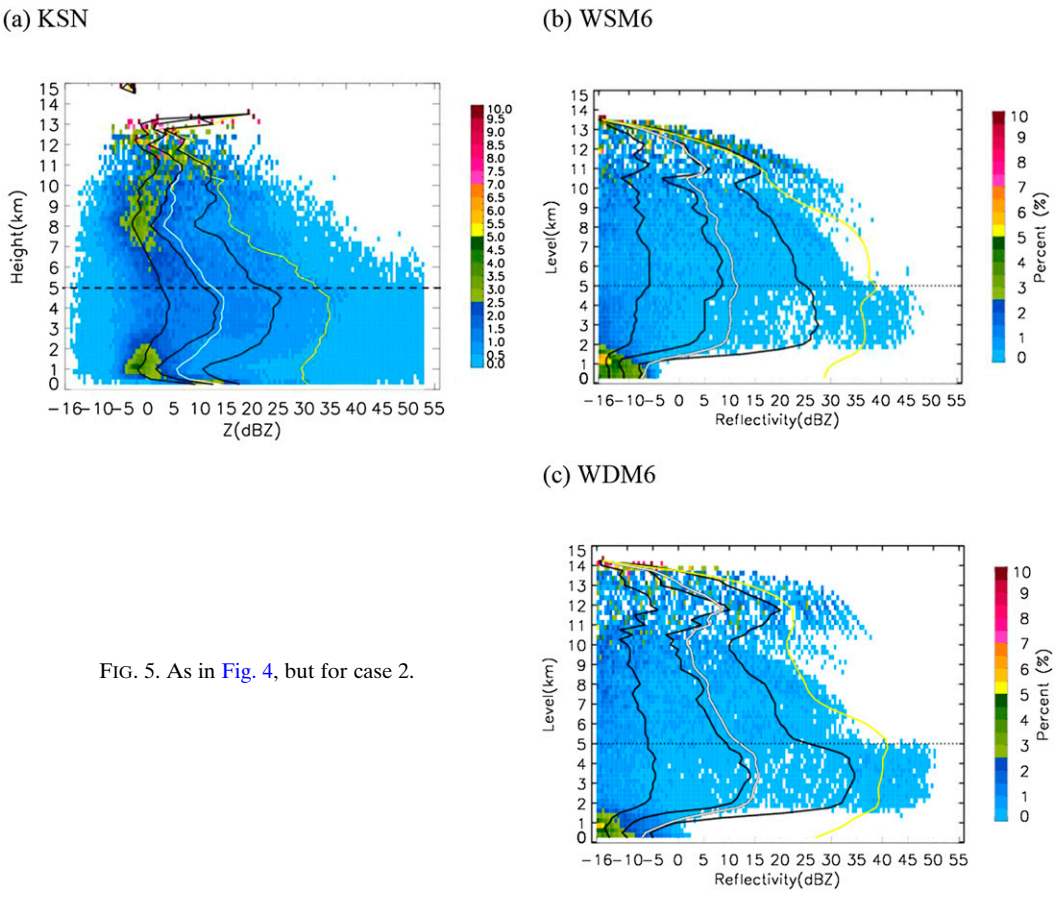

FIG. 5. As in Fig. 4, but for case 2.

frequency interval and 250-m vertical spacing (Figs. 3–6). The cumulative reflectivity frequencies of the 25th, 50th, and 75th percentiles are marked with black solid lines, the average reflectivity (dBZ) is marked by the white solid line, and the average of the reflectivity factor in linear units ($mm^{-6} m^{-3}$) is marked by the yellow solid line for each height. The linear average puts more weight on the high reflectivity value than the logarithmic mean (white curve), and in areas where a surge of reflectivity exists such as at the BB, the graph appears more drastic. Thus, the BB location can be identified more easily.

Figure 3 represents the CFAD for GDK-observed results (Fig. 3a) and WSM6 (Fig. 3b) and WDM6 (Fig. 3c) simulations. The x axis is reflectivity, the y axis shows altitude, and the color pixels represent the frequency percentage of reflectivity for the given height. Pixels with the highest value of 10% are colored red. The dashed line shows the 0°C isotherm layer for comparison between the radar and the WRF simulations using the two schemes. For the GDK site in case 1, the radar BB is located near 4.5 km and the level of the 0°C isotherm layer is at about 4.7 km (Fig. 3a), according to S.-H. Lee (2012). The two WRF simulations using WSM6 and WDM6 do not show a clear signature for the BB location. The peak reflectivity of the WSM6 simulation occurs near 5 km but the modeled 0°C isotherm layer is at 4.8 km (Fig. 3b). For the WDM6 simulation, the peak reflectivity varies from 4 to 5 km and there seems to be no clear signature of BB, even though the 0°C isotherm layer is the same as that of the WSM6 simulation (Fig. 3c). However, when comparing the mean profile of reflectivity (white solid line) and the 50% line, WDM6 tends to simulate higher reflectivity (centered near 20 dBZ) compared to WSM6 (centered near 10 dBZ) and matches more closely the observed radar profile of 20 dBZ below the BB. WSM6 simulates reflectivity that is too weak when compared to WDM6 and the radar reflectivity below the melting layer. WDM6, however, simulates stronger reflectivity than the radar profile at 75% and the linear average reflectivity factor (yellow solid line).

The CFAD of the KSN radar site and simulations of WSM6 and WDM6 are shown in Fig. 4. The radar bright band is located near 4.5 km, similar to that of the GDK site (Fig. 4a). However, the slope of the

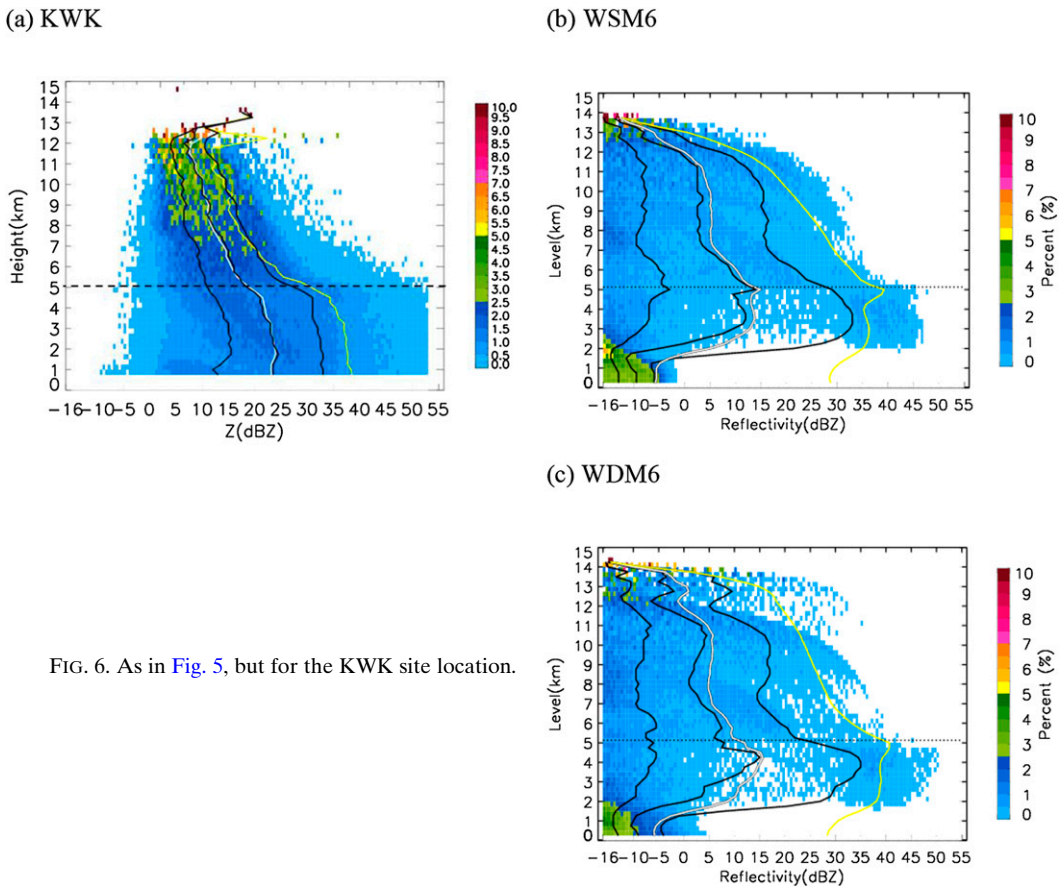

FIG. 6. As in Fig. 5, but for the KWK site location.

reflectivity changes drastically above the BB and a nose-tailed profile with a high peak is seen at 4.5 km, indicating that a significant melting of ice occurred at this layer. The reflectivity peaks for WSM6 and WDM6 occur near 5 km where the 0°C melting levels exist (Figs. 4b,c). There is about a 500-m difference in the location of the 0°C melting level, meaning that the two schemes simulated the melting of ice-phase hydrometeors at levels that were too high when compared to radar observations. A similar trend for the GDK site can be found between WSM6 and WDM6 when comparing reflectivity fields below the melting layer. WDM6 shows a mean reflectivity field that more closely matches that of the radar, whereas WSM6 shows reflectivity fields that are too weak at lower levels.

The scattered convection case (case 2) is shown in Figs. 5 and 6. The observed precipitation from the AWS shows that the convection band is located along the western coast and to the northwest of South Korea but the model-simulated precipitation band is located at the center of South Korea (see Fig. 2). The results for KSN and KWK are shown for comparison. The radar precipitation band for the KSN site is not as concentrated as in case 1 and there are widespread echoes at low levels (Fig. 5a). The BB is typically not observed for convective precipitation because of the strong vertical mixing between the hydrometeors. However, GDK showed a BB at around 4.8 km as a result of trailing stratiform precipitation behind the major convective band as the system entered into the decaying stage (figure not shown). The radar 0°C isotherm layer was estimated from the GDK CFAD. For KSN, there is a slight peak in reflectivity near 4.5 km and the mean reflectivity below this level is about 10 dBZ. The peak reflectivities of WSM6 and WDM6 are not distinguishable and both show reduced reflectivity below 2 km (Figs. 5b,c). Furthermore, the schemes have reflectivities concentrated at around −16 dBZ, close to the surface, indicating that the model failed to simulate the convective precipitation for case 2. However, the simulated 0°C isotherm layer is similar to that obtained from the radar.

The CFAD of the KWK site and simulations of WSM6 and WDM6 for case 2 are shown in Fig. 6. Again, the radar 0°C isotherm layer was estimated from the GDK CFAD. There is a gradual increase in the peak of reflectivity from 12 to 1 km indicating significant growth of droplets by cold and warm rain processes. The mean

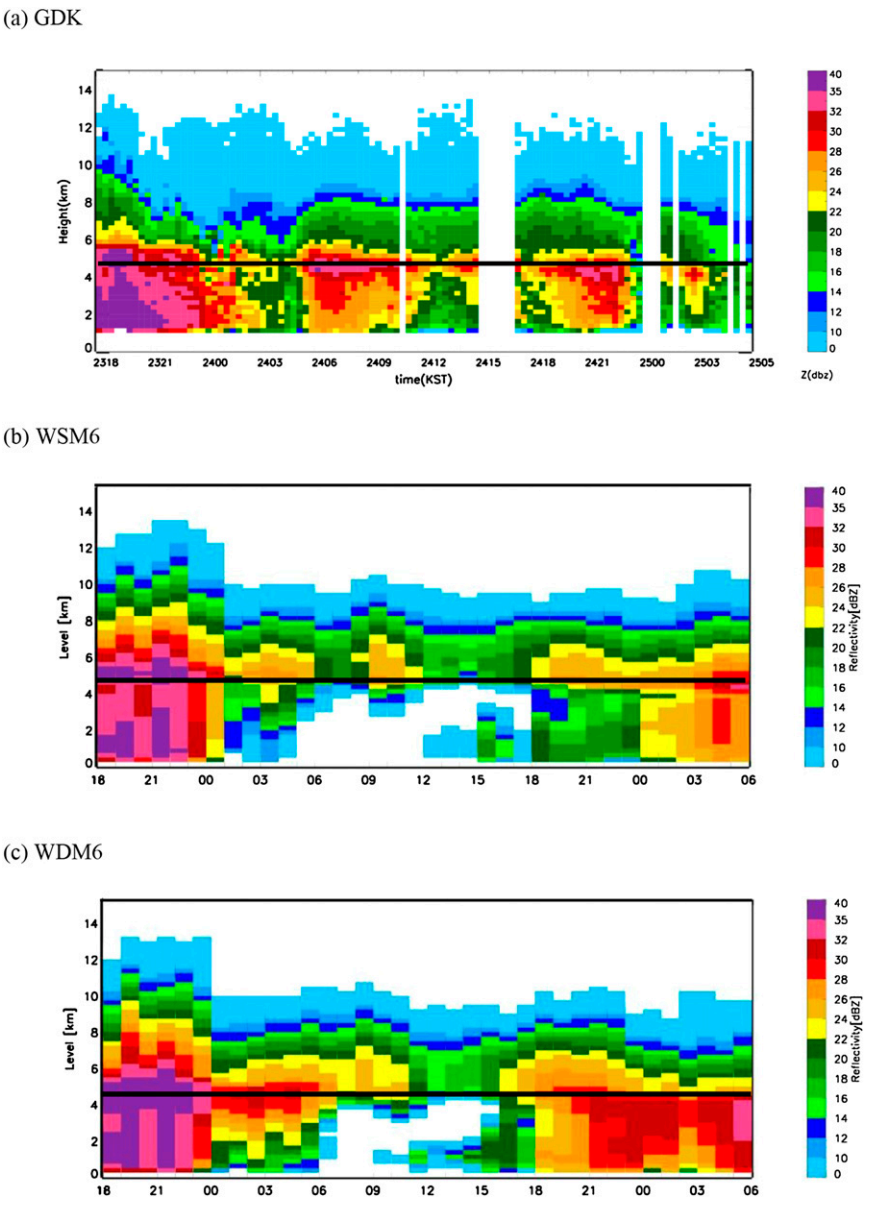

FIG. 7. Time–height cross sections of (a) GDK-observed and (b) WSM6- and (c) WDM6-simulated radar reflectivities for case 1.

reflectivity below 5 km is about 20–25 dBZ (Fig. 6a). For WSM6 and WDM6, the peak reflectivity is located near 4–5 km (Figs. 6b,c). Although the simulated 0°C isotherm layer is similar to that obtained from the radar, both schemes fail to produce strong reflectivity near the ground surface indicating the model had difficulty in simulating convective precipitation during this period.

b. *Time–height cross sections*

Time–height cross sections are shown in Figs. 7–11. The time–height cross sections of radar observations have 20-min temporal resolution whereas WSM6 and WDM6 have 1-h resolution. However, all three datasets were interpolated to 250-m vertical resolution from their native polar and sigma vertical coordinates. The range is limited to a 100-km radius for the reasons provided in section 2d. The BB in the time–height cross section is represented by a line that stretches horizontally with higher reflectivity than the neighboring area. It is useful to identify the duration of the precipitation and the varying echo tops of the precipitating system. It is used to augment CFAD, which does not reveal time evolution characteristics of

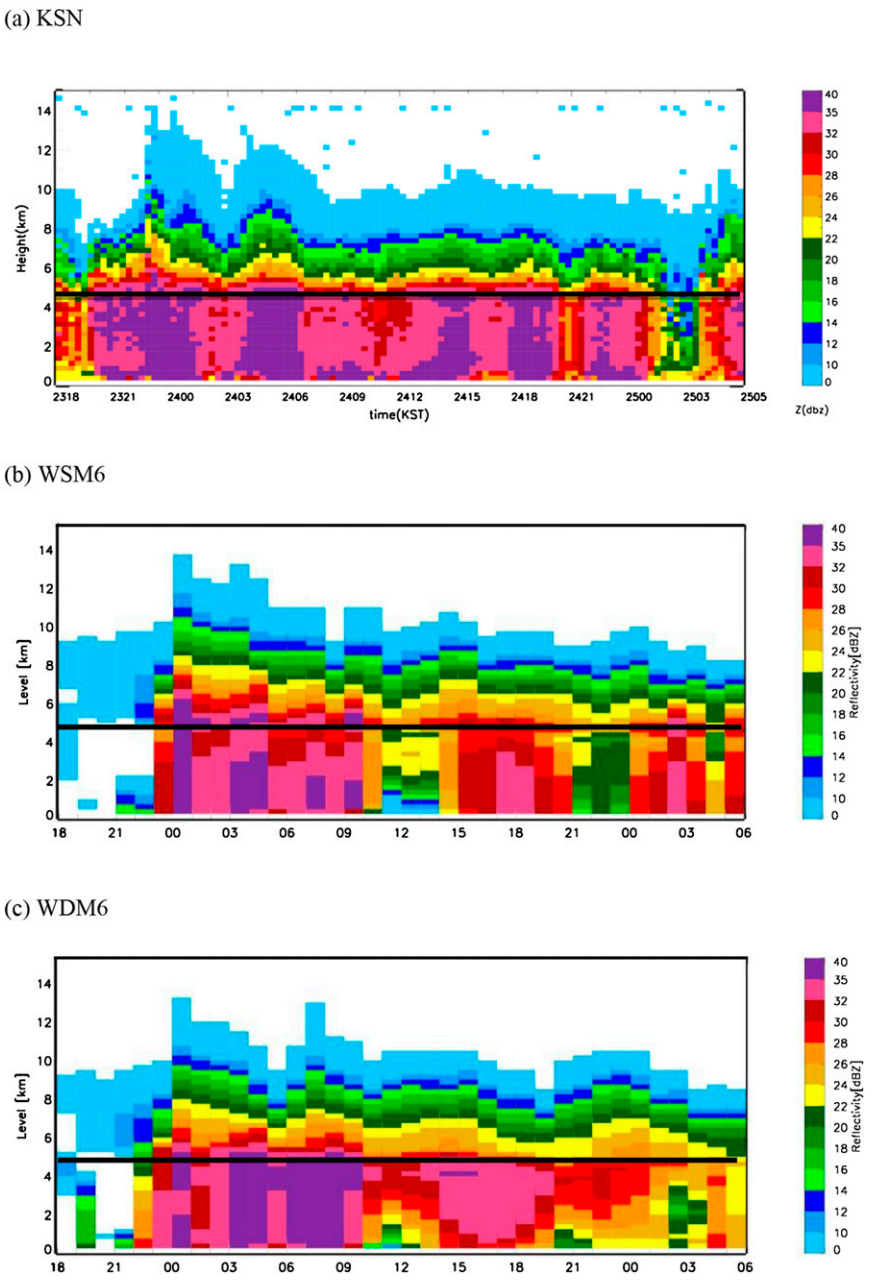

FIG. 8. As in Fig. 7, but for the KSN site location.

precipitation that are related to phase errors in simulating storms. Figure 7 shows time–height cross sections for the GDK site location. The solid line represents the 0°C isotherm layer obtained from radar observations, as well as from WSM6 and WDM6. In the radar cross section, the peak in reflectivity is below the 0°C isotherm for most of the time (Fig. 7a), but for WSM6 and WDM6, there are no such systematically identifiable features (Figs. 7b,c). Neither WSM6 nor WDM6 produced the stratiform precipitation between 0600 and 1200 UTC 24 June 2011, and the precipitation in the final quarter of the period was overestimated. For KSN (Fig. 8), there is generally good agreement in timing the precipitation, except for the first 3–4 h of the simulation period. WDM6 simulates slightly stronger reflectivity than WSM6, which is in better agreement with the radar cross section. The enhanced reflectivity or precipitation of WDM6 is attributed to the double-moment calculation of number concentrations for cloud, rainwater, and CCN. This allows WDM6 to account for

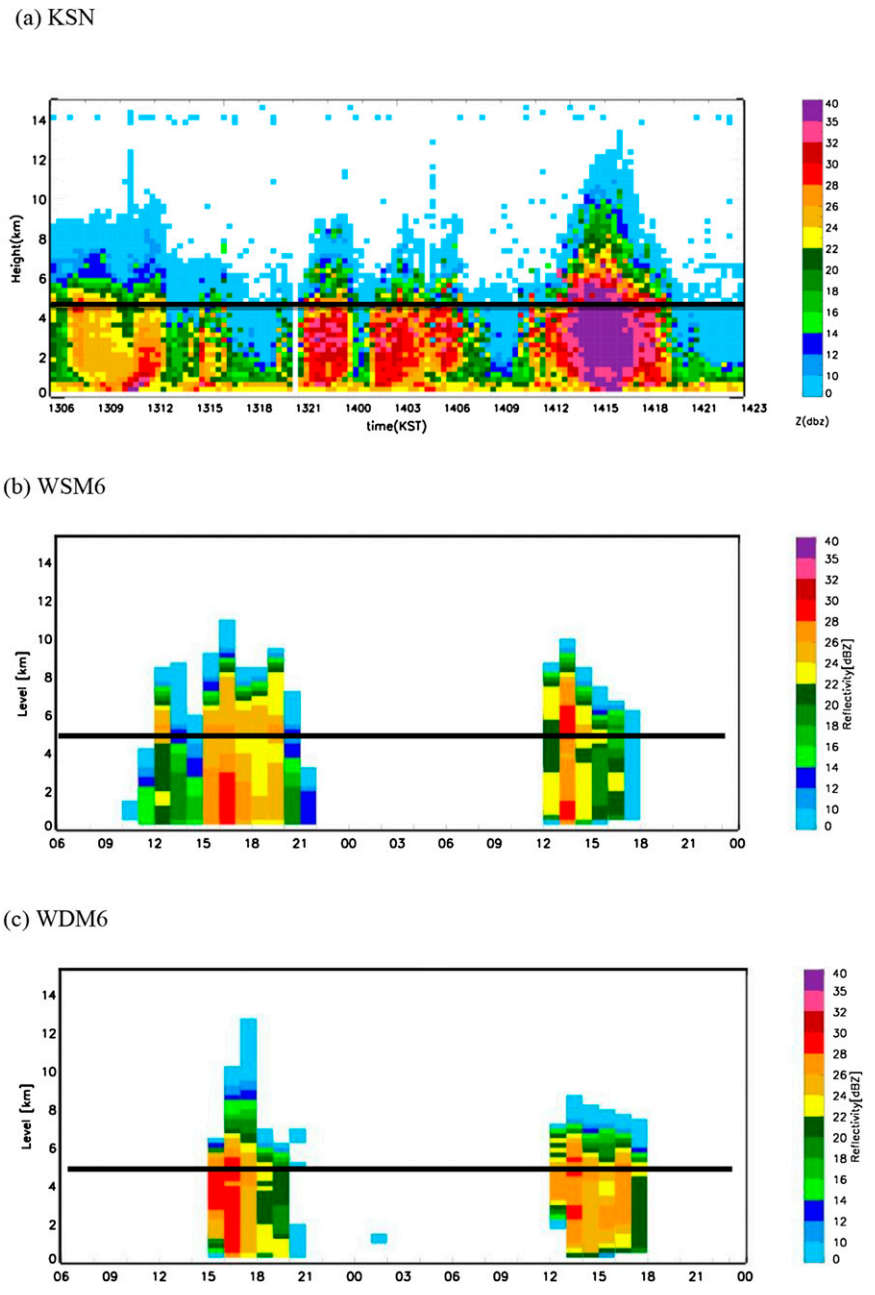

FIG. 9. As in Fig. 8, but for case 2.

the sedimentation process of raindrops whereas WSM6 does not.

The time–height cross sections for the KSN and KWK site locations for case 2 are shown in Figs. 9 and 10. Again, the radar melting level is estimated from the GDK CFAD, which showed a BB. For the two site locations, WSM6 and WDM6 model the afternoon [1200–2100 Korea standard time (KST)] convective precipitation fairly well but fail to produce late hour and early morning (0000–1200 KST) convective precipitation during this period. Interestingly, there exists strong resolution dependence in simulating some of the convective precipitation, and the 12-km resolution runs of domain 2 are depicted in Fig. 11 for comparison. The strongest convective precipitation, with an echo top of 14 km that occurred during the afternoon of 14 August 2011, is not simulated by either of the schemes with 12-km horizontal resolution. For both resolution runs, WDM6 shows reflectivity increasing toward the ground, whereas WSM6 does not as a result of the lack of double-moment treatment in the scheme. The CFAD and

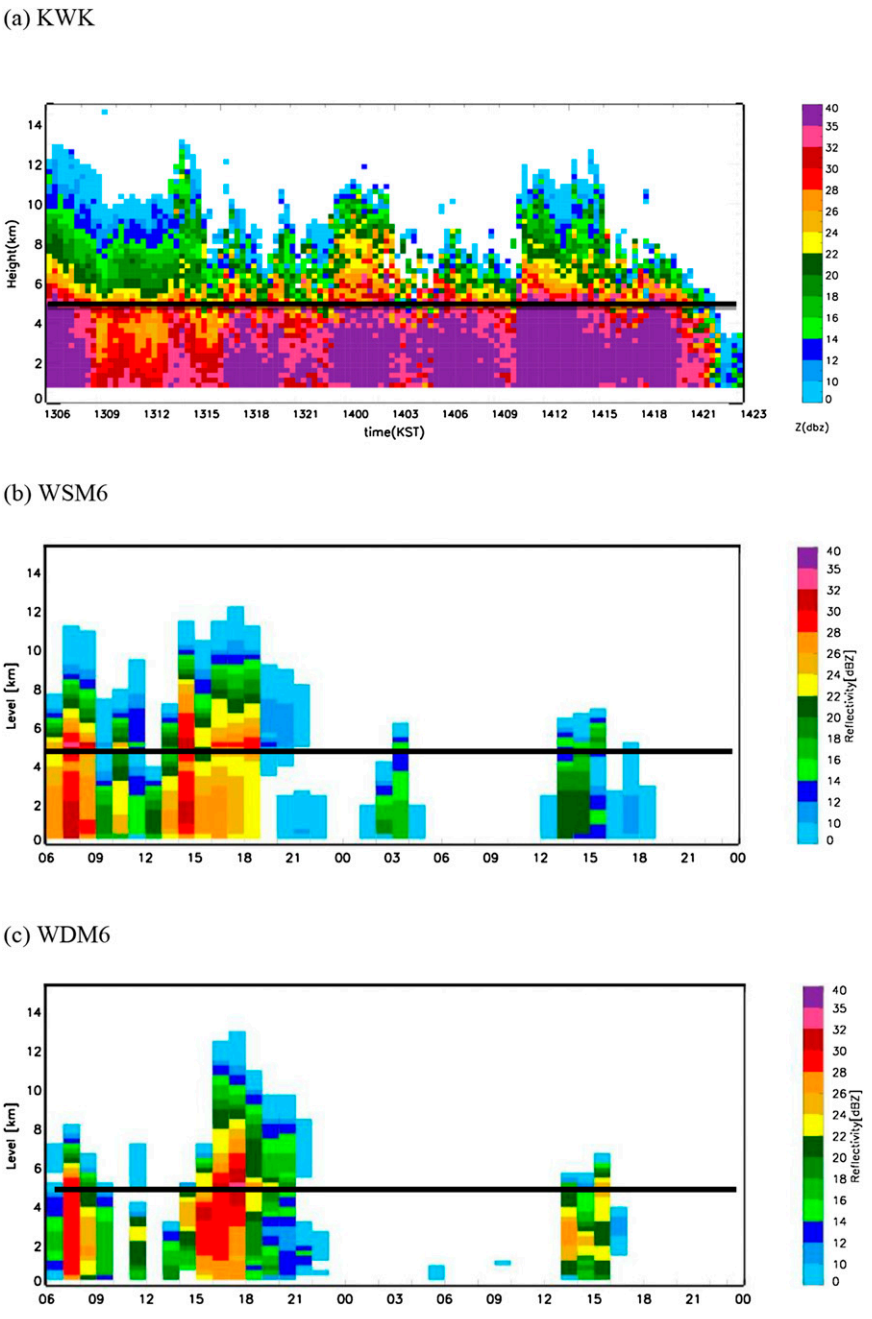

FIG. 10. As in Fig. 9, but for the KWK site location.

time–height cross section for the summer monsoon case with 12-km resolution were similar to those for 4 km (figure not shown), but the time–height cross section for the convective case showed marked differences. To have any skill in simulating convective precipitation in the region, a grid spacing of 4 km or higher is necessary.

c. *Vertical profiles*

In Fig. 12, the vertical profiles of temperature, relative humidity, and hydrometeors for case 1 (summer monsoon case) are shown for WSM6 and WDM6 at the GDK (Figs. 12a,b) and KSN (Figs. 12c,d) sites. The solid curve represents WSM6 and the dashed curve represents the WDM6 simulation. The two temperature curves (red lines) are almost identical between the two schemes, but WDM6 has a slightly higher relative humidity (blue curves) of about 5% below the 0°C melting level of 5 km as compared to WSM6 (Figs. 12a,c). The most noticeable differences are found in the hydrometeor predictions (Figs. 12b,d).

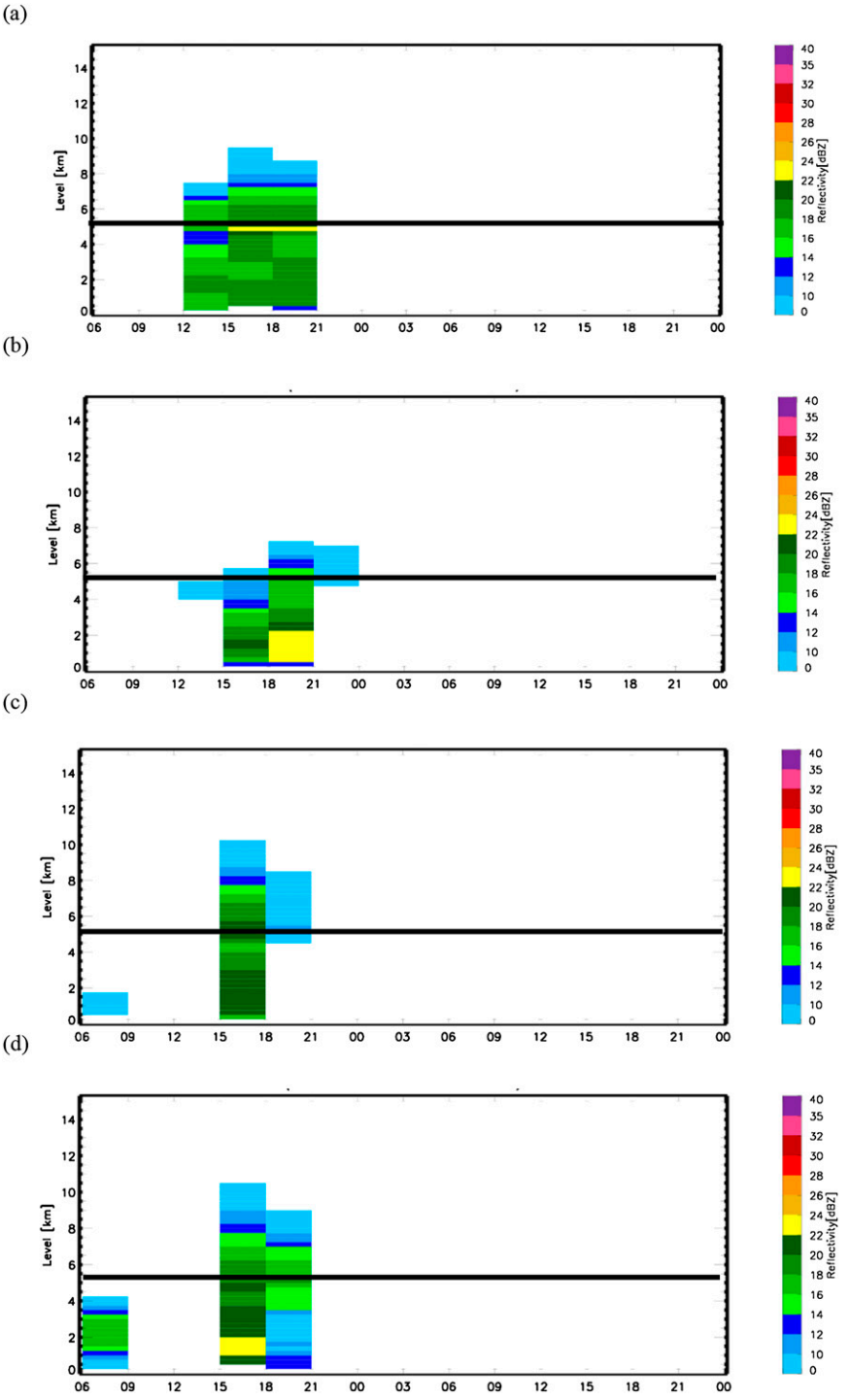

FIG. 11. Time–height cross sections for 12-km-resolution simulation of case 2 at (a),(b) KSN and (c),(d) KWK for the WSM6 and WDM6 simulations, respectively.

Above the melting layer, the specific humidity of ice-phase particles such as ice (i.e., q_{ice}), snow (i.e., q_{snow}), and graupel (i.e., q_{graupel}) are quite similar with respect to its average amount, whereas liquid-phase particles of cloud (i.e., q_{cloud}) and rain (i.e., q_{rain}) show large discrepancies. In particular, the specific humidity of rain is twice as large ($0.17\,\text{g}\,\text{kg}^{-1}$ vs $0.08\,\text{g}\,\text{kg}^{-1}$ for GDK and $0.22\,\text{g}\,\text{kg}^{-1}$ vs $0.12\,\text{g}\,\text{kg}^{-1}$ for

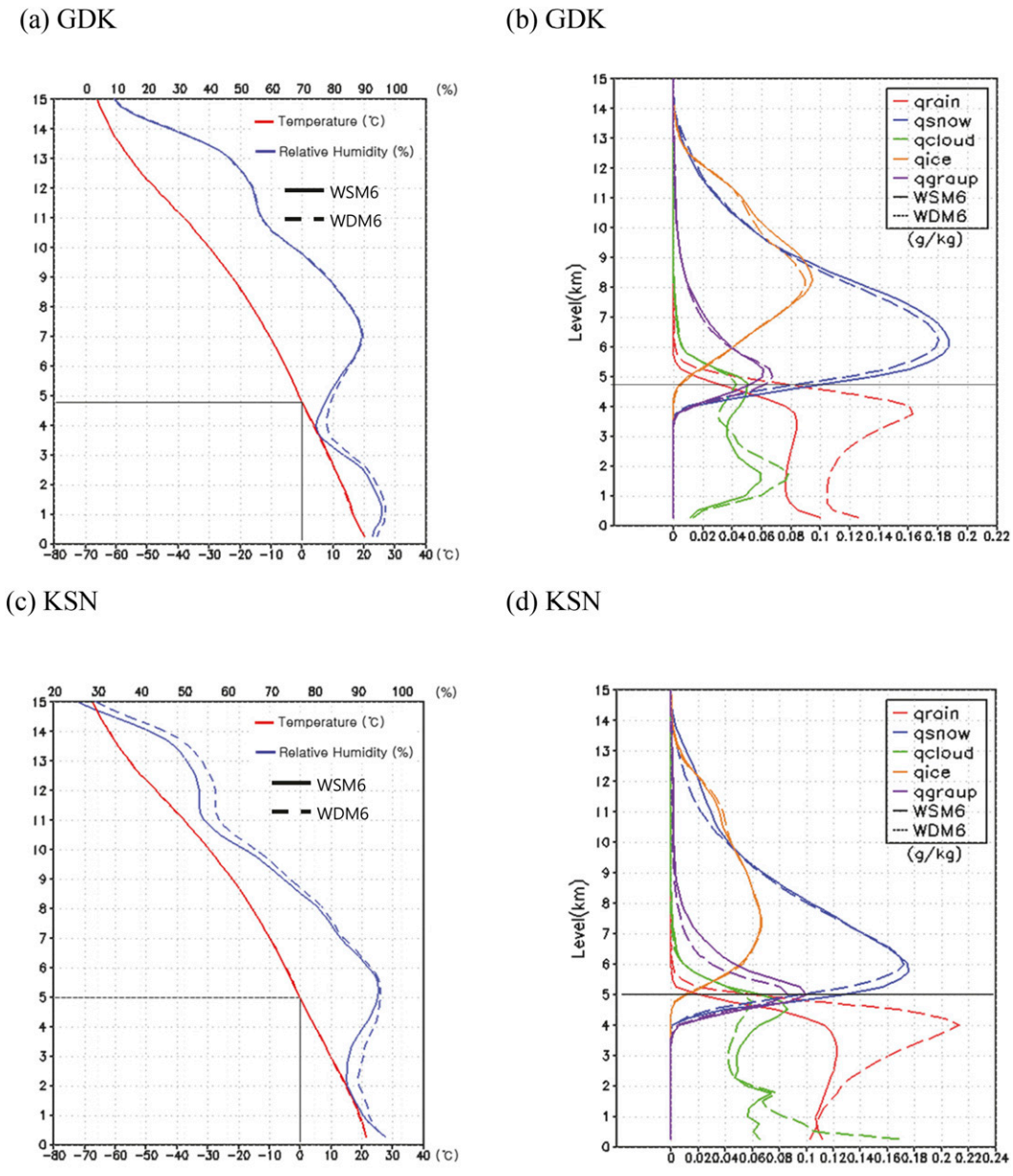

FIG. 12. Vertical profiles of (a),(c) temperature and relative humidity and (b),(d) hydrometeors from WSM6 and WDM6 for (top) GDK and (bottom) KSN in case 1. Solid lines are for WSM6 and dashed lines are for WDM6.

KSN) in the WDM6 simulations. The reason for the higher reflectivity in CFAD of WDM6 is due to the difference in q_{rain}. For the convective precipitation profile, the temperature profiles are not distinguishable between the two schemes (Fig. 13a), but the relative humidity is slightly higher in WDM6 (Fig. 13c). Because both schemes had problems in simulating scattered precipitation during this period, more cloud is simulated than rain, as revealed in the hydrometeor profile (Figs. 13b,d).

Therefore, the accuracy of WDM6 over WSM6 when compared to radar observations can be attributed to the difference in the sedimentation process simulated by the second moment of number concentrations with liquid-phase particles. This in turn creates larger raindrops and increases the relative humidity beneath the melting layer, allowing WDM6 to simulate a more realistic reflectivity profile than does WSM6. However, for the convective case, both schemes underestimate the precipitation and there is resolution dependence in

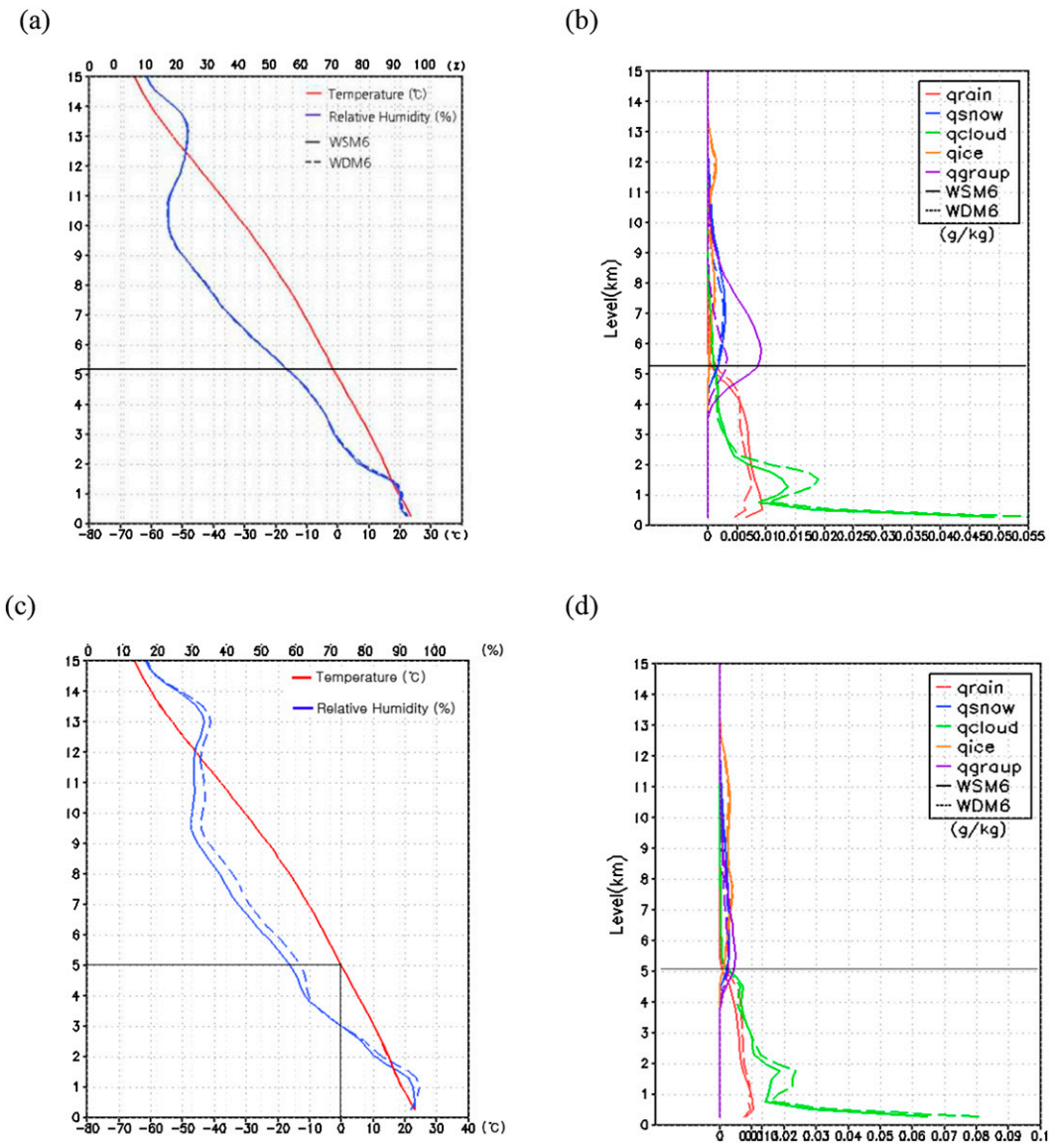

FIG. 13. As in Fig. 12, but for case 2 at KSN and KWK.

the WRF Model's ability to simulate convective-type precipitation. Table 4 summarizes the statistics of the BB height and the 0°C isotherm layer (in parenthesis) obtained from radar observations and WSM6 and WDM6 for all four cases. As shown in the statistics, both schemes have a tendency to overestimate the location of the melting layer and BB height when compared to radar observations.

TABLE 4. Summary statistics of radar and the WSM6 and WDM6 BB height and 0°C melting level (in parentheses) for three radar sites used in this study. Units are kilometers.

		Case 1	Case 2	Case 3	Case 4	Mean
Avg height	Radar	4.43 (4.63)	4.8 (5.0)	4.9 (5.1)	—	4.71 (4.91)
	WSM6	4.67 (4.97)	— (5.2)	5.0 (5.3)	— (5.2)	4.84 (5.17)
	WDM6	4.53 (4.8)	— (5.23)	5.0 (5.17)	— (5.2)	4.77 (5.1)
Bias of 0°C melting level	Radar	—	—	—	—	—
	WSM6	0.24 (0.34)	— (0.2)	0.1 (0.2)	—	(0.25)
	WDM6	0.1 (0.17)	— (0.23)	0.1 (0.07)	—	(0.16)

4. Summary and conclusions

We used the ARW, version 3.5, and selected four cases for evaluating WSM6 and WDM6. Cases 1 and 3 were for the summer monsoon known as the changma front in Korea that occurred toward the end of June and into early July 2011. Cases 2 and 4 were for scattered convection events that occurred after the end of the summer monsoon in mid-August as a result of atmospheric instability. We compared the melting layer and BB signatures obtained from ground-based S-band Doppler radar with WSM6 and WDM6 that will be adapted in the KGM.

Comparison of the contoured frequency by altitude diagram (CFAD) and time–height cross sections are utilized to assess the two schemes in simulating the summer monsoon and convective precipitation cases. To understand the microphysics mechanism responsible for the differences in the two schemes, we further investigated the vertical profiles of hydrometeors and temperature with humidity profiles. Radar data are quality controlled using a fuzzy logic algorithm developed at KNU to remove AP and nonmeteorological echoes such as ground clutter, sea clutter, and chaffs.

The results show that for the two monsoon cases, WSM6 shows a systemic bias of simulating smaller reflectivity values beneath the melting layer when compared to radar data, while WDM6 has a tendency to simulate higher reflectivity. For the convective cases, there is still room for improvement for modeling the height of the melting level, hydrometeor types, and various precipitation aspects (timing, location, intensity, etc.) in model simulations. Overall, WSM6 and WDM6 have a tendency to overestimate the location of the melting level and the BB height when compared to the radar observations. The accuracy of WDM6 over WSM6 when compared to the radar observations can be attributed to the difference in the sedimentation process simulated by the second moment of number concentrations of liquid-phase particles. This in turn creates larger raindrops and increases the relative humidity beneath the melting layer, allowing WDM6 to simulate a more realistic reflectivity profile than WSM6. The melting of snow or ice below the freezing level is determined by the air saturation below the level. Matsuo and Sasyo (1981) reported that the depth of the nonmelting layer increased linearly as relative humidity decreased as a result of the cooling of snow or ice by sublimation of water vapor. Thus, most of the model error can be attributed to the mixing ratio of the hydrometeors. However, for the convective case, both schemes significantly underestimate the precipitation amount and there is resolution dependence in the WRF Model's ability to simulate convective-type precipitation.

It is important to note that it is not possible to make a strict comparison between reflectivity computed from a model grid point and that measured by ground-based radar. The radar resolution degrades with range. Radars cannot detect hydrometeors in the lower atmosphere as a result of the earth's curvature effect, as well as numerous other considerations (ground clutter, AP, bright bands, etc.). Furthermore, the simulated reflectivity is bound to the accuracy of the model cloud and precipitation microphysics forecast, since it is derived directly from the hydrometeor humidity. Any biases in the specific humidity will be reflected in the SR field because of the diameter-to-the-sixth-power dependence of the equivalent reflectivity factor. This dependence renders reflectivity highly sensitive to the largest precipitation particles present, and causes the simulated reflectivity to be highly sensitive to the precipitation mixing ratios and also to assumptions about the precipitation size distributions. It is conceivable that a model could be performing well in terms of the precipitation forecast, but producing unrealistic SR fields due to poor representation of the particle size distributions. Thus, direct comparisons between the model-simulated reflectivity fields and radar measurements are susceptible to problems.

Finally, this study shows the possibility of utilizing radar data to validate a mesoscale model's output and cloud microphysics schemes in detail. The results obtained herein can help to fine-tune the cloud microphysical schemes and eventually improve the performance and accuracy of numerical weather prediction models. More case studies will be conducted in the future to generalize our study results using radar and model data.

Acknowledgments. This study was funded by the Korea Meteorological Administration Research and Development Program under Grant KMIPA 2015-1090. The authors thank the Korea Institute of Atmospheric Prediction Systems (KIAPS) for their research support and the KNU radar team for their technical support in processing radar data. We also thank the anonymous reviewers for their constructive comments, which led to an improved manuscript.

REFERENCES

Austin, P. M., and A. C. Bemis, 1950: A quantitative study of the "bright band" in radar precipitation echoes. *J. Meteor.*, **7**, 145–151, doi:10.1175/1520-0469(1950)007<0145:AQSOTB>2.0.CO;2.

Chepfer, H., S. Bony, D. Winker, M. Chiriaco, J.-L. Dufresne, and G. Seze, 2008: Use of *CALIPSO* lidar observations to evaluate the cloudiness simulated by a climate model. *J. Geophys. Res.*, **35**, L15704, doi:10.1029/2008GL034207.

Cho, Y. H., G. Lee, K.-E. Kim, and I. Zawadzki, 2006: Identification and removal of ground echoes and anomalous propagation using the characteristics of radar echoes. *J. Atmos. Oceanic Technol.*, **23**, 1206–1222, doi:10.1175/JTECH1913.1.

Fabry, F., and I. Zawadzki, 1995: Long-term radar observations of the melting layer of precipitation and their interpretation. *J. Atmos. Sci.*, **52**, 838–851, doi:10.1175/1520-0469(1995)052<0838:LTROOT>2.0.CO;2.

Haynes, J. M., R. T. Marchand, Z. Luo, A. Bodas-Salcedo, and G. L. Stephens, 2007: A multipurpose radar simulation package: QuickBeam. *Bull. Amer. Meteor. Soc.*, **88**, 1723–1727, doi:10.1175/BAMS-88-11-1723.

Hitchens, N. M., M. E. Baldwin, and R. J. Trapp, 2012: An object-oriented characterization of extreme precipitation–producing convective systems in the midwestern United States. *Mon. Wea. Rev.*, **140**, 1356–1366, doi:10.1175/MWR-D-11-00153.1.

Hong, S.-Y., and J.-O. J. Lim, 2006: The WRF single-moment 6-class microphysics scheme (WSM6). *J. Korean Meteor. Soc.*, **42**, 129–151.

——, J. Dudhia, and S.-H. Chen, 2004: A revised approach to ice microphysical processes for the bulk parameterization of clouds and precipitation. *Mon. Wea. Rev.*, **132**, 103–120, doi:10.1175/1520-0493(2004)132<0103:ARATIM>2.0.CO;2.

——, K.-S. Lim, Y.-H. Lee, J.-C. Ha, H.-W. Kim, S.-J. Ham, and J. Dudhia, 2010: Evaluation of the WRF double-moment 6-class microphysics scheme for precipitating convection. *Adv. Meteor.*, **2010**, 707253, doi:10.1155/2010/707253.

Kain, J. S., and Coauthors, 2008: Some practical considerations regarding horizontal resolution in the first generation of operational convection-allowing NWP. *Wea. Forecasting*, **23**, 931–952, doi:10.1175/WAF2007106.1.

Koch, S. E., B. Ferrier, M. Stoelinga, E. Szoke, S. J. Weiss, and J. S. Kain, 2005: The use of simulated radar reflectivity fields in the diagnosis of mesoscale phenomena from high-resolution WRF Model forecasts. Preprints, *11th Conf. on Mesoscale Processes/32nd Conf. on Radar Meteorology*, Albuquerque, NM, Amer. Meteor. Soc., J4J.7. [Available online at https://ams.confex.com/ams/pdfpapers/97032.pdf.]

Konsta, D., H. Chepfer, and J. L. Dufresne, 2012: A process oriented description of tropical oceanic clouds for climate model evaluation, based on a statistical analysis of daytime A-train high spatial resolution observations. *Climate Dyn.*, **39**, 2091–2108, doi:10.1007/s00382-012-1533-7.

Kwon, H., J. S. Kang, Y. Jo, and J. H. Kang, 2014: Implementation of a GPS-RO data processing system for the KIAPS-LETKF data assimilation system. *Atmos. Meas. Tech. Discuss.*, **7**, 11 927–11 956, doi:10.5194/amtd-7-11927-2014.

Lee, G., 2012: *Integrated Quality Control Technology of Radar Data at Kyungpook National University*. Weather Radar Center, KMA, 305 pp.

Lee, S.-H., 2012: Detection of bright band and analysis of its characteristics using the KMA weather radar data. M.S. thesis, Dept. of Astronomy and Atmospheric Sciences, Kyungpook National University, 88 pp.

Lim, K.-S. S., and S.-Y. Hong, 2010: Development of an effective double-moment cloud microphysics scheme with prognostic cloud condensation nuclei (CCN) for weather and climate models. *Mon. Wea. Rev.*, **138**, 1587–1612, doi:10.1175/2009MWR2968.1.

Liu, H., and V. Chandrasekar, 2000: Classification of hydrometeors based on polarimetric radar measurements: Development of fuzzy logic and neuro-fuzzy systems, and in situ verification. *J. Atmos. Oceanic Technol.*, **17**, 140–164, doi:10.1175/1520-0426(2000)017<0140:COHBOP>2.0.CO;2.

Matsuo, T., and Y. Sasyo, 1981: Melting of snowflakes below freezing level in the atmosphere. *J. Meteor. Soc. Japan*, **59**, 10–25.

Molthan, A. L., and B. A. Colle, 2012: Comparisons of single- and double-moment microphysics schemes in the simulation of a synoptic-scale snowfall event. *Mon. Wea. Rev.*, **140**, 2982–3002, doi:10.1175/MWR-D-11-00292.1.

Morrison, H., and A. Gettelman, 2008: A new two-moment bulk stratiform cloud microphysics scheme in the Community Atmosphere Model, version 3 (CAM3). Part I: Description and numerical tests. *J. Climate*, **21**, 3642–3659, doi:10.1175/2008JCLI2105.1.

Seo, D.-J., J. Breidenbach, R. Fulton, D. Miller, and T. O'Bannon, 2000: Real-time adjustment of range-dependent biases in WSR-88D rainfall estimates due to nonuniform vertical profile of reflectivity. *J. Hydrometeor.*, **1**, 222–240, doi:10.1175/1525-7541(2000)001<0222:RTAORD>2.0.CO;2.

Skamarock, W. C., and Coauthors, 2008: A description of the Advanced Research WRF version 3. NCAR Tech. Note NCAR/TN-475+STR, 113 pp. [Available online at http://www2.mmm.ucar.edu/wrf/users/docs/arw_v3.pdf.]

Smith, C. J., 1986: The reduction of errors caused by bright bands in quantitative rainfall measurements made using radar. *J. Atmos. Oceanic Technol.*, **3**, 129–141, doi:10.1175/1520-0426(1986)003<0129:TROECB>2.0.CO;2.

Smith, R. N. B., 1990: A scheme for predicting layer clouds and their water content in a general circulation model. *Quart. J. Roy. Meteor. Soc.*, **116**, 435–460, doi:10.1002/qj.49711649210.

Smyth, T. J., and A. J. Illingworth, 1998: Radar estimates of rainfall rates at the ground in bright band and non-bright band events. *Quart. J. Roy. Meteor. Soc.*, **124**, 2417–2434, doi:10.1002/qj.49712455112.

Stewart, R. E., J. D. Marwitz, J. C. Pace, and R. E. Carbone, 1984: Characteristics through the melting layer of stratiform clouds. *J. Atmos. Sci.*, **41**, 3227–3237, doi:10.1175/1520-0469(1984)041<3227:CTTMLO>2.0.CO;2.

Stoelinga, M. T., 2005: Simulated equivalent reflectivity factor as currently formulated in RIP: Description and possible improvements. University of Washington Tech. Rep., 5 pp. [Available online at http://www.atmos.washington.edu/~stoeling/RIP_sim_ref.pdf.]

Sun, J., and N. A. Crook, 1997: Dynamical and microphysical retrieval from Doppler radar observations using a cloud model and its adjoint. Part I: Model development and simulated data experiments. *J. Atmos. Sci.*, **54**, 1642–1661, doi:10.1175/1520-0469(1997)054<1642:DAMRFD>2.0.CO;2.

Sundqvist, H., 1978: A parametrization scheme for non-convective condensation including prediction of cloud water content. *Quart. J. Roy. Meteor. Soc.*, **104**, 677–690, doi:10.1002/qj.49710444110.

Thompson, G., P. R. Field, R. M. Rasmussen, and W. D. Hall, 2008: Explicit forecasts of winter precipitation using an improved bulk microphysics scheme. Part II: Implementation of a new snow parameterization. *Mon. Wea. Rev.*, **136**, 5095–5115, doi:10.1175/2008MWR2387.1.

Wilson, D. R., and S. P. Ballard, 1999: A microphysically based precipitation scheme for the UK Meteorological Office Unified Model. *Quart. J. Roy. Meteor. Soc.*, **125**, 1607–1636, doi:10.1002/qj.49712555707.

Wright, D. M., D. J. Posselt, and A. L. Steiner, 2013: Sensitivity of lake-effect snowfall to lake ice cover and temperature in the Great Lakes region. *Mon. Wea. Rev.*, **141**, 670–689, doi:10.1175/MWR-D-12-00038.1.

Ye, B.-Y., 2012: Quality control of radar moment data by combining moment-based fuzzy logic algorithm and radar signal processing. M.S. thesis, Dept. of Astronomy and Atmospheric Sciences, Kyungpook National University, 72 pp.

Yuter, S. E., and R. A. Houze, 1995: Three-dimensional kinematic and microphysical evolution of Florida cumulonimbus. Part II: Frequency distributions of vertical velocity, reflectivity, and differential reflectivity. *Mon. Wea. Rev.*, **123**, 1941–1963, doi:10.1175/1520-0493(1995)123<1941:TDKAME>2.0.CO;2.

Zawadzki, I., A. Bellon, C. Côté, and F. Fabry, 2001: Target identification by dual-polarization radar in an operational environment. Preprints, *30th Int. Conf. on Radar Meteorology*, Munich, Germany, Amer. Meteor. Soc., 2B.5. [Available online at https://ams.confex.com/ams/pdfpapers/21568.pdf.]